Journal of Alloys and Compounds 519 (2012) 29–36

Contents lists available at SciVerse ScienceDirect

Journal of Alloys and Compounds

journal homepage: www.elsevier.com/locate/jallcom

Key insights on the structural characterization of textured Er_2O_3–ZrO_2 nano-oxides prepared by a surfactant-free solvothermal route

Beatriz Julián-López[a,*], Verónica de la Luz[a], Francisco Gonell[a], Eloisa Cordoncillo[a], Miguel López-Haro[b], Jose J. Calvino[b], Purificación Escribano[a,1]

[a] Departamento de Química Inorgánica y Orgánica, Universitat Jaume I, Avda. Vicente Sos Baynat s/n, 12071 Castellón, Spain
[b] Departamento de Ciencia de los Materiales e Ingeniería Metalúrgica y Química Inorgánica, Facultad de Ciencias, Universidad de Cádiz, Campus Rio San Pedro, Puerto Real, 11510 Cádiz, Spain

ARTICLE INFO

Article history:
Received 5 September 2011
Received in revised form
17 November 2011
Accepted 22 November 2011
Available online 9 December 2011

In memoriam of Prof. Purificación Escribano, passed away on November 24th 2011.

Keywords:
Structural resolution
Er_2O_3–ZrO_2
HRTEM
Fluorite
Solvothermal route

ABSTRACT

Zirconia-mixed oxides can exhibit cubic fluorite and pyrochlore structure. Their discrimination is not easy in nanooxides with a crystal size close to that of a few unit cells. In this work, high resolution transmission electron microscopy (HRTEM) has been employed to provide key insights on the structural characterization of a nanometric and porous mixed Er_2O_3–ZrO_2 oxide. The material was prepared by a simple template-free solvothermal route that provided nanocrystalline powders at low temperature (170 °C) with spherical morphology, and high surface area (~280 $m^2 g^{-1}$). The porosity was mainly originated from the assembling of organic complexing agents used in the synthesis to limit the crystal growth and to control hydrolysis and condensation reaction rates. The samples were characterized by thermal analysis, X-ray diffraction, scanning electron microscopy and N_2 adsorption measurements.

A detailed study by HRTEM was conducted on microtomed samples. It was observed that the material was made of nanocrystals packed into spherical agglomerates. HRTEM simulations indicated that it is not possible to identify the pyrochlore phase in nanoparticles with diameter below 2 nm. In our samples, the analysis of the HRTEM lattice images by means of fast Fourier transform (FFT) techniques revealed well defined spots that can be assigned to different planes of a cubic fluorite-type phase, even in the raw material. Raman spectroscopy was also a powerful technique to elucidate the crystalline phase of the materials with the smallest nanoparticles. HREM and Raman results evidenced that the material is constituted, irrespective of the temperature of the final calcination step, by an ensemble of randomly oriented nanocrystals with fluorite structure. This study opens new perspectives for the design of synthetic approaches to prepare nanooxides (fluorites and pyrochlores) and the analysis of their crystalline structure.

1. Introduction

One of the biggest challenges for scientists working in the field of nanomaterials is to perform an accurate structural and chemical characterization of the system. The classical characterization techniques such as X-ray diffraction (XRD), scanning and transmission electron microscopy (SEM and TEM, respectively), and so on, have strong limitations when the size of the nanomaterial is close to that of a few unit cells. This point is exceptionally important in the case of materials whose crystalline phase is dependent on the particle size. An important family of materials with this particular situation is ZrO_2 and its derivates.

Zirconia-based nanoceramics are attractive for a variety of applications, such as solid-oxide fuel cells, three-way catalysts, oxygen sensors or refractory materials [1–6]. Most of these applications make use of size-dependent properties of zirconia nanocrystals. Therefore, the precise control of the particle size, the crystalline phase, morphology, textural properties and lattice defects (anionic vacancies, etc.) is absolutely required.

Pure ZrO_2 exists in three polymorphic structures: monoclinic, tetragonal and cubic. In general, the increasing temperature stabilizes more symmetrical phases. Thus, the phase transformation usually takes place from monoclinic to cubic. Doping zirconia with trivalent cations [7] promotes the formation of oxygen vacancies for charge compensation. This can favour sevenfold coordinated oxygen ions around the Zr cations and stabilize tetragonal or cubic phases at low temperature [8–10].

The structural modifications may impact the electronic structure of the lattice, and then, useful physico-chemical properties could emerge. It is well known, for instance, the enhancement of

* Corresponding author. Fax: +34 964 728214.
E-mail address: julian@qio.uji.es (B. Julián-López).
[1] Deceased.

0925-8388/$ – see front matter © 2011 Elsevier B.V. All rights reserved.
doi:10.1016/j.jallcom.2011.11.099

mechanical and electrical properties of yttria-stabilized zirconia. Lanthanide-doped zirconia has also great potential for solid-state photonic applications. Indeed, ZrO_2 is one of the best candidates as host matrix for luminescent ions due to its chemical and photochemical stability, high refractive index and low phonon energy.

When Zr(IV) is substituted by Ln(III) cations, a pyrochlore structure with a cubic *Fd*−3*m* symmetry can be developed. The pyrochlore lattice is closely related to that of fluorite, ZrO_2 (space group *Fm*−3*m*), but with ordered cations and ordered vacancies in 1/8 of the tetrahedral anion sites. Indeed, pyrochlore ($A_2B_2O_7$, with A: La^{3+}, Y^{3+}, Ce^{3+}, Sm^{3+}, etc. and B: Zr^{4+}, Ti^{4+}, Hf^{4+}, etc.) can be considered as a superstructure of an anion-deficient fluorite atomic arrangement that is originated at high temperatures through a progressive disordering-to-ordering transition from the fluorite structure (formulae $A_{0.5}B_{0.5}O_{1.75}$) [11]. The stability of pyrochlore phase depends on the radii of A and B cations, but different ranges of stability for pyrochlore phase have been reported in the literature. For instance, Bevan et al. [12] have established that the superstructure of the pyrochlore is stable in compounds with radii r_A/r_B ratio of 1.2–1.6; but Thomson et al. [13] give r_A/r_B values between 1.46 and 1.8. The origin of these uncertainties could be found in the particle size of the materials studied, which can modify the stability of the crystalline phase.

The control over the crystalline phase (fluorite, defect fluorite, pyrochlore, etc.) and the extent of oxygen vacancies is crucial for their applications in SOFC, catalysis, sensors, and so on [14–16] because each phase exhibits different properties. For instance, rare-earth doped zirconia in the cubic fluorite structure is inherently more radiation resistant in radiation damage experiments than in the pyrochlore phase [16]. Thus, the crystalline phase is a key factor to analyze the chemical durability and radiation tolerance of potential hosts for actinides and radioactive wastes.

The synthetic strategies usually employed in solid-state chemistry (ceramic route) do not lead themselves to such controlled synthesis. *Chimie Douce* strategies can offer one approach to target synthesis, providing new and predictable structures. These nanocrystalline and metastable compounds can exhibit unusual electrical, magnetic and optical properties [17]. In these nanomaterials, the main point is to make an accurate study of their crystal structure. It usually requires the use of advanced instrumental techniques such as high resolution transmission electron microscopy (HRTEM). This technique has been used to determine the structure of ceria–zirconia systems [18a] because cerium ions can exhibit two oxidation states and these materials can develop pyrochlore (Ce^{3+}) or polymorphs like fluorite structure (if cerium ions are mainly as Ce^{4+}).

The studies about lanthanide zirconates are mainly restricted to ceria–zirconia systems for their interest in catalysis. In this report, we focus on erbia–zirconia mixed oxide that finds interesting applications as radiation-resistant material [16], and potentially in catalysis or photonics. Therefore, the purpose of this research is to find a general route to prepare porous and nanocrystalline lanthanide zirconates by a non-aqueous and template-free methodology, and also provide new insights in their characterization. In particular, solvothermal synthesis has been selected as an adequate route to prepare porous nanocrystals of erbia–zirconia mixed oxide in a single step, at low-temperature, and avoiding the use of surfactants as templates. The key factor of this approach is the incorporation of a complexing agent (acetylacetone) that controls the hydrolysis and condensation rates and also acts as a structure directing agent.

The non-aqueous and simple conditions employed in this synthetic strategy allow the material to be prepared with specific features in terms of crystalline phases, size, morphology and also textural properties. Special attention is paid to determine the crystalline phase of the material due to their interest for further

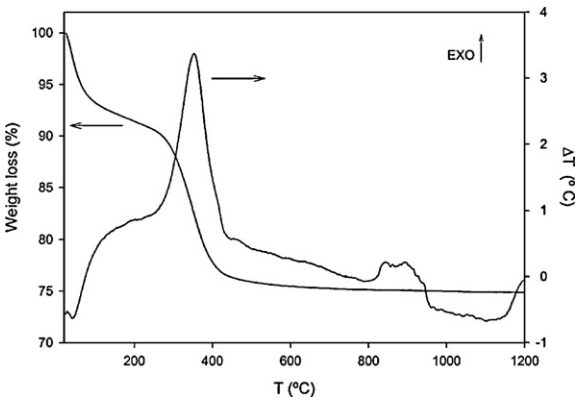

Fig. 1. Thermal behaviour of raw erbium–zirconium oxide sample.

applications. The goal of this study is to increase the knowledge about lanthanide zirconates stability and give a light on the previously mentioned difficulties. Structural, morphological and textural characterizations have been performed by XRD, SEM, HRTEM, SAED, Raman spectroscopy and N_2 sorption techniques.

2. Results and discussion

The thermal stability of the raw Er–Zr oxide is shown in Fig. 1. The DTA-TG curves show that raw material contains 25% in weight of organic matter that decomposes in two steps, one at around 100 °C (water and solvents physically adsorbed) and 300–400 °C (combustion of organic moieties coming from acetylacetone and alkoxide groups). At around 800–950 °C a broad exothermic signal without mass loss is detected. This can be attributed to a rearrangement of defects in the lattice. However, this is not the only possibility: they have been observed in processes of phase transformation from fluorite to pyrochlore [19]. In the erbia–zirconia system, the ratio of Er(III) and Zr(IV) radii is in the limit of stability between both structures. Then, other techniques such as XRD, HRTEM and Raman experiments will be necessary to clarify this point.

X-Ray diffraction patterns (XRD) of the raw sample (solvothermal treatment at 170 °C) and after annealing at different temperatures (400 °C, 550 °C, 800 °C and 1200 °C) are depicted in Fig. 2.

The XRD profiles show broad diffraction peaks at around 30°, 34°, 50° and 60° that become narrower with increasing temperature. The low intensity and broadness of the XRD reflexions for the as-synthesized sample (170 °C) indicates that the powder is

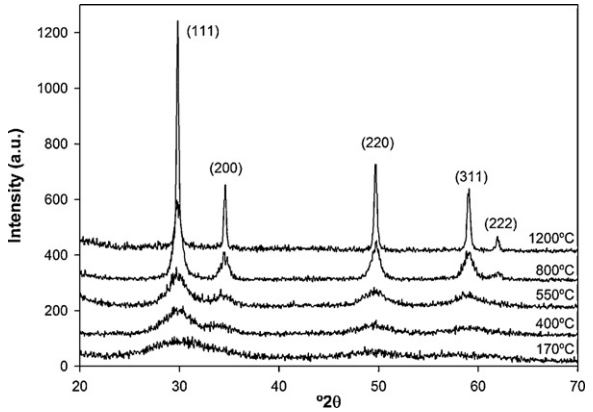

Fig. 2. X-ray diffraction patterns of erbia–zirconia at (a) 170 °C, (b) 400 °C, (c) 550 °C, (d) 800 °C and (e) 1200 °C.

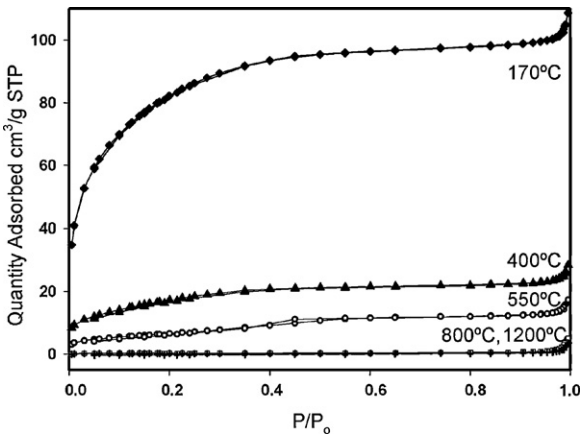

Fig. 3. N_2 adsorption–desorption isotherms of the material annealed at different temperatures.

amorphous or nanocrystalline. This feature is maintained up to 550 °C, where the crystalline character becomes evident. It is also worth noting that the crystallite size is maintained in the nanometric range at temperatures such as 1200 °C, as further determined by Scherrer's equation.

The pattern of the sample annealed at 800 °C reveals defined peaks that can be assigned to {1 1 1}, {2 0 0}, {2 2 0}, {3 1 1} and {2 2 2} planes of cubic $Er_{0.5}Zr_{0.5}O_{1.75}$ compound (JCPDS 78-1299). However, due to the width of the peaks, the pattern could also be coincident with a tetragonal or cubic ZrO_2 structure (JCPDS 42-1164 or 49-1642, respectively), or even defective fluorites such as $ZrO_{1.87}$ (JCPDS 081-1551). In any of these phases, Er^{III} ions would be located in Zr^{IV} positions and oxygen vacancies would be originated for charge compensation. What it is confirmed from the XRD pattern at 800 °C is the absence of the 1/2 (1 1 1) reflection at around 15° characteristic of the pyrochlore $Er_2Zr_2O_7$ lattice (superstructure derived from fluorite). This point is of great interest for the further application of the material.

The sample was annealed at higher temperature (1200 °C) in order to increase crystallization and improve the peak's assignation. In this way, we can also discard tetragonal ZrO_2 because no splitting on some reflexions ({2 0 0}, {2 2 0} and {3 1 1}) was detected.

It is highlighted that X-ray diffraction technique has important limitations in determining the crystalline structure of nanocrystals. Concretely, it is very difficult to make an accurate description of the crystalline phases at temperatures at which the crystalline domains are in the order of a few nanometers. Therefore, other techniques such as high resolution transmission electron microscopy and Raman spectroscopy are necessary to go deep into this study, as shown further.

The average crystallite size of the samples was estimated from the full width at the half maximum (FWHM) of the most intense (1 1 1) diffraction peak, using the Scherrer equation [20] with a correction for instrument line broadening (quartz as pattern). The size of the crystalline domains, assuming spherical morphology, is shown in Table 1. They are in the range of a few nanometers at moderated temperatures, 1–4 nm, and increases up to ~30 nm at high temperature (1200 °C). These small sizes at such a high temperature are of great interest in catalysis and sensors.

Textural properties of the materials were analyzed by N_2 adsorption–desorption measurements. The isotherms are shown in Fig. 3. The adsorption–desorption curve of the raw sample (170 °C) might be classified as type I [21]. The type I isotherms are reversible and characteristic of microporous solids having small external surfaces (e.g. activated carbons, molecular sieve zeolites and certain porous oxides) [21]. In general, the pore-filling mechanisms are dependent on the pore shape and are influenced by the properties of the adsorptive gas and the adsorbent–adsorbate interactions. In our case, the limiting uptake is mostly being governed by the accessible micropore volume rather than by the internal surface area. The calculation of Brunauer–Emmett–Teller specific surface area (S_{BET}) gave a value of around 280 $m^2\,g^{-1}$ (Table 1). This high surface is surprising because the sample contains a significant amount of residual organic matter (detected from thermogravimetric analysis). This value is much higher than other mixed oxides prepared by solvothermal route without the help of surfactants or templates [22–24].

The samples annealed at higher temperatures result in adsorption isotherms with similar profiles but lower specific surface area (Table 1) and total adsorbed volume (Fig. 3). This behaviour is due to the removal of organic moieties and the subsequent sintering processes of nanocrystals. Despite of the reduction in textural properties, high S_{BET} values are preserved at temperatures at which organic matter is almost decomposed (~62 $m^2\,g^{-1}$ at 400 °C), what can be of interest for some applications (catalysis, oxygen sensors, SOCF, etc.).

The isotherm of the sample heated at 550 °C shows a type IV nature with the characteristic hysteresis loop at relatively low P/P^0. This profile can be due to onset coarsening and coalescence of nanoparticles to form cylindrical pores. This hysteresis is associated with capillary condensation taking place in mesopores, and desorbing preferably at 0.42 relative pressure. Taking into account that organic moieties are completely removed, and the average size estimated by Scherrer equation of nanoparticles are around 4 nm, it is reasonable to expect void spaces between nanoparticles with distance end to end close to 2 nm (in the limit of micro- and mesoporosity according to IUPAC statements). In addition, it is known that hysteresis loops at relative low pressure depends not only on the nature of the sample but also on the nature of the adsorptive gas. Thus, for nitrogen at its boiling point, the desorption gap at $P/P^0 = 0.42$ corresponds to a pore radius of ca. 3 nm (according to Kelvin equation [21]). These results are consistent with those obtained from XRD measurements and Scherrer calculations.

The samples annealed at 800 and 1200 °C show adsorption curves characteristic of non-porous materials (see Fig. 3, isotherms are overlapped). At these temperatures, the porosity is almost negligible due to the sintering process of nanoparticles.

The morphology of the sample and its evolution with temperature was examined by scanning electron microscopy (SEM). The image shown in Fig. 4a corresponds to the as-synthesized sample. This powder consists on individual particles with spherical morphology and diameters ranging from 200 nm to 3 μm. These sub-micrometric particles are constituted by agglomerates of small nanoparticles (see bumpy texture in Fig. 4b). The agglomeration process takes place during the solvothermal treatment. In order to reduce this effect and to homogenize the particle size, experiments with different reaction time were performed but the results were not completely satisfactory. By reducing reaction time to 12 h, still some particles of micrometric size (not shown) were detected. The decrease of reagents concentration could be also another strategy to reduce the size of particles but the amount of final product would be small, and the process would be less profitable. Therefore, if the further application requires an accurate calibration of the particle size, a simple and inexpensive decantation process would be necessary.

An interesting feature of the material is that it exhibits a rough surface (Fig. 4b). This bumpy texture would be consistent with the fact that these spherical sub-micrometric particles are made of small nanocrystals that agglomerate during solvothermal treatment into a bigger structure of low surface energy. These nanocrystals are responsible for the width of XRD patterns.

Table 1
Average crystallite size and textural parameters of the sample calculated from XRD measurements and N_2 adsorption/desorption isotherms.

Thermal treatment	Crystallite size (nm)	S_{BET} ($m^2\ g^{-1}$)	Pore volume ($cm^3\ g^{-1}$)	Pore size (nm)
Raw (170 °C)	1.2	282.7	0.060	2.7
400 °C	2.6	61.9	0.016	3.0
550 °C	3.8	24.3	0.078	6.0
800 °C	8.8	1.0	–	–
1200 °C	32.9	0.5	–	–

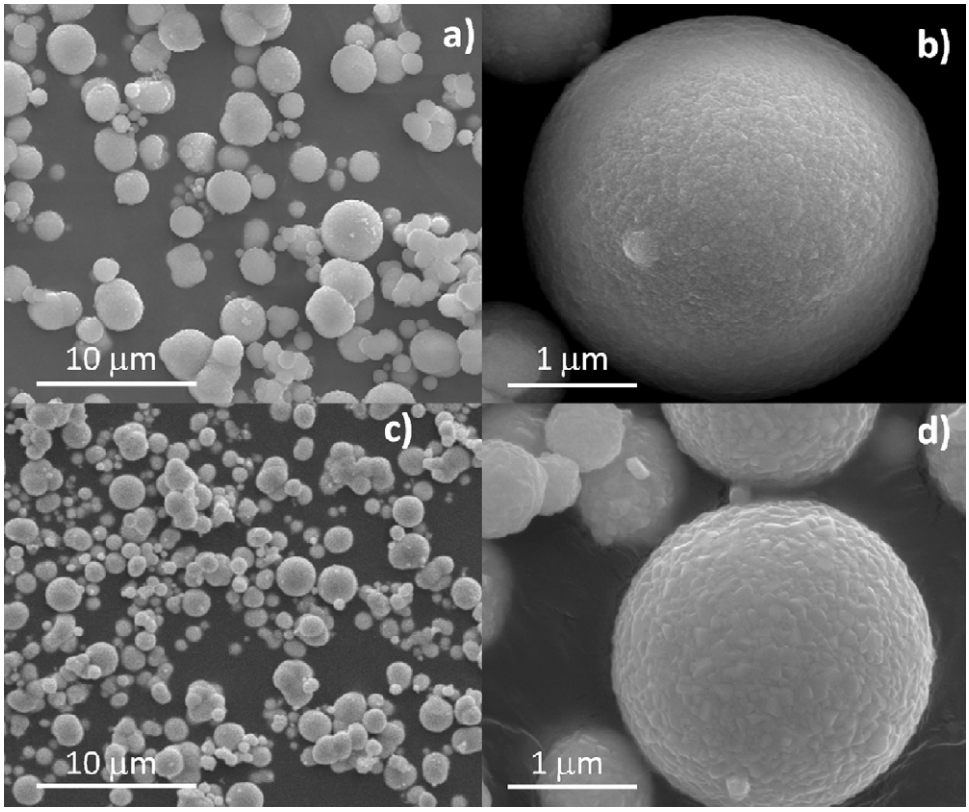

Fig. 4. SEM micrographs at different magnifications (1200× and 25,000×) of the Er–Zr oxide: as-synthesized (a and b) and after firing at 1200 °C (c and d).

Fig. 4c reveals that morphology does not change significantly with increasing temperature. The most significant change is the shrinkage of the microspheres, reducing their volume between 15% and 30%. An estimation of the particle-size distribution has been performed by counting and measuring the diameter of the microspheres. Graphics are shown in supplementary information section, and reveals a maximum in the size distribution located at 1.4 μm for the raw sample (170 °C) that shifts to 0.8 μm after treatment at 1200 °C. This effect is certainly due to the loss of organic matter and the thermal sintering of nanocrystals. Despite of the material contraction, the surface roughness is still observed (Fig. 4d), even some polyhedral features in the surface can be detected. In Scheme 1, there is a representation of the material that could explain the evolution of the mesostructure with temperature.

Elemental composition of all the samples was studied by using energy-dispersive X-ray (EDX) analysis in the scanning electron microscope. It was confirmed the homogeneous distribution of heavy elements (Er and Zr atoms) in all the analyzed regions (not shown), and also that the composition was very close to the stoichiometry of the fluorite $Er_{0.5}Zr_{0.5}O_{1.75}$ structure.

HRTEM measurements were performed to go deep into the structural characterization. The main interest was to confirm if the structure detected by XRD corresponded to cubic $Er_{0.5}Zr_{0.5}O_{1.75}$ fluorite or to other structures (tetragonal-derived ZrO_2, pyrochlore lattice, etc.). Pyrochlore (P) and fluorite (F) are closely related structures. In the literature, we find many examples of lanthanide zirconates $Ln_2Zr_2O_7$ exhibiting both structures: pyrochlores when

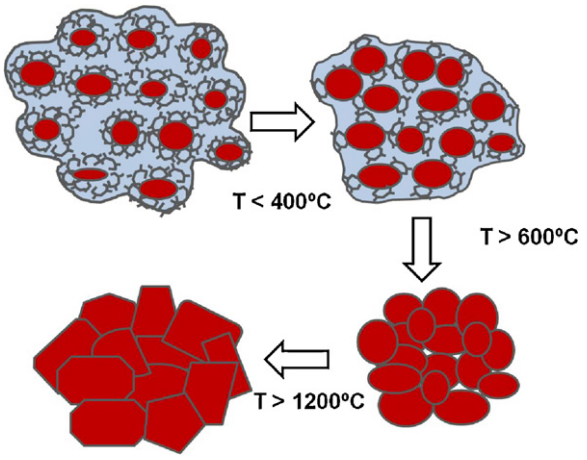

Scheme 1. Schematic representation of the evolution of material's structure with thermal treatment: nanocrystals in red and organic matter in blue.

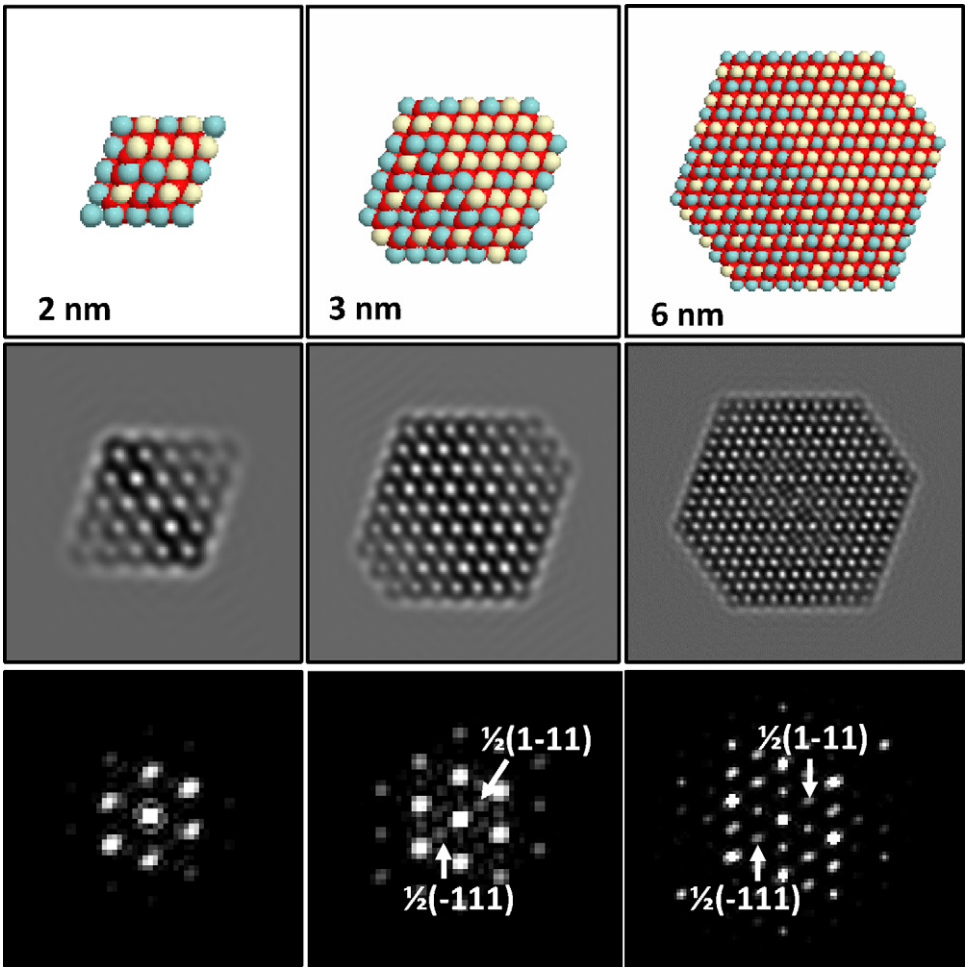

Fig. 5. (Top row) Structural models used for the simulations. (Middle row) simulated HRTEM images for $Er_2Zr_2O_7$ pyrochlore nanostructures modelled in the top row (accelerating voltage 200 kV, C_s 1 mm, spread of focus 10 nm, Δf 81 nm). (Bottom row) DDPs obtained for these calculations. Extra reflections are marked with an arrow.

Ln^{3+} is Sm^{3+} [25]; Ce^{3+} [18b]; La^{3+} or Nd^{3+} [26,27]; fluorite when Ln^{3+} is La^{3+}, Eu^{3+} or Y^{3+} [26]; or mixed phases for Gd^{3+} [25–27].

Pyrochlore is a superstructure derived from fluorite, an extra reflection at 1/2 $\{1\,1\,1\}_F$ would be observed in XRD and also HRTEM techniques. The lattice spacings of these extra reflections are just double that of the fluorite cell from which it is derived, and are due to the cation-ordering effect which takes place in the pyrochlore. Absence of such additional reflection is a clear indication of the fluorite formation. In our samples, the absence of this reflection has been confirmed in micrometric crystal sizes (samples annealed at 800 °C and 1200 °C), as already mentioned in the XRD section. However, in nanoparticles, where the crystalline domains are in the order of a few unit cells, the detection of this extra reflection is not easy.

Therefore, the question was whether the size of the crystallites is so small that such extra reflection could not be effectively detected in the HRTEM images. To address this issue, we have performed a HTREM image simulation study. For this purpose, we modelled a set of $Er_2Zr_2O_7$ nanoparticles with pyrochlore structure of increasing diameter, in the range observed in our samples (2–6 nm), Fig. 5.

Using the electronooptical parameters of the JEOL2100 LaB_6 microscope in which the experimental HRTEM images were recorded, we obtained the calculated images of these nanoparticles. Fig. 5 middle row shows the calculations along the [1 1 0] zone axis of the structure. Fig. 5 bottom row shows the digital diffraction patterns (DDPs) of the calculated images. It is interesting to notice that for the smallest particle, 2 nm, the 1/2 {1 1 1} reflections cannot be seen. In the case of the 3 nm particle the visibility of such reflections is still low, but for the larger particle, 6 nm, all the extra reflections can be easily detected. The same conclusions could be drawn from images calculated at other defocus values. Thus, we can conclude from these calculations that, in a microscope with the electronooptical characteristics of that used in the present study, for the smallest sizes, roughly below 3 nm, discrimination between the fluorite and the pyrochlore structure is out of reach from HRTEM images. Nevertheless, for larger crystals, the appearance of these extra spots is a fingerprint of the transition from fluorite to pyrochlore. Image simulation data reported recently about the size detection limit of the pyrochlore phase in other lanthanide–Zr pyrochlores [18] using a microscope of higher resolution, coincide well with those reported here.

From these results, HRTEM images and selected area electron diffraction (SAED) measurements of the critical samples were performed. Fig. 6 shows representative images of the microtomed samples after thermal treatments at 170 °C, 400 °C and 550 °C. The samples annealed at 800 °C and 1200 °C were not analyzed by HRTEM because the experimental data undoubtedly pointed out the development of cubic $Er_{0.5}Zr_{0.5}O_{1.75}$ fluorite.

Fig. 6 shows well defined, nanosized, particles in the three cases, packed into larger agglomerates. These images are in agreement with the structure proposed in Scheme 1, and it would explain the

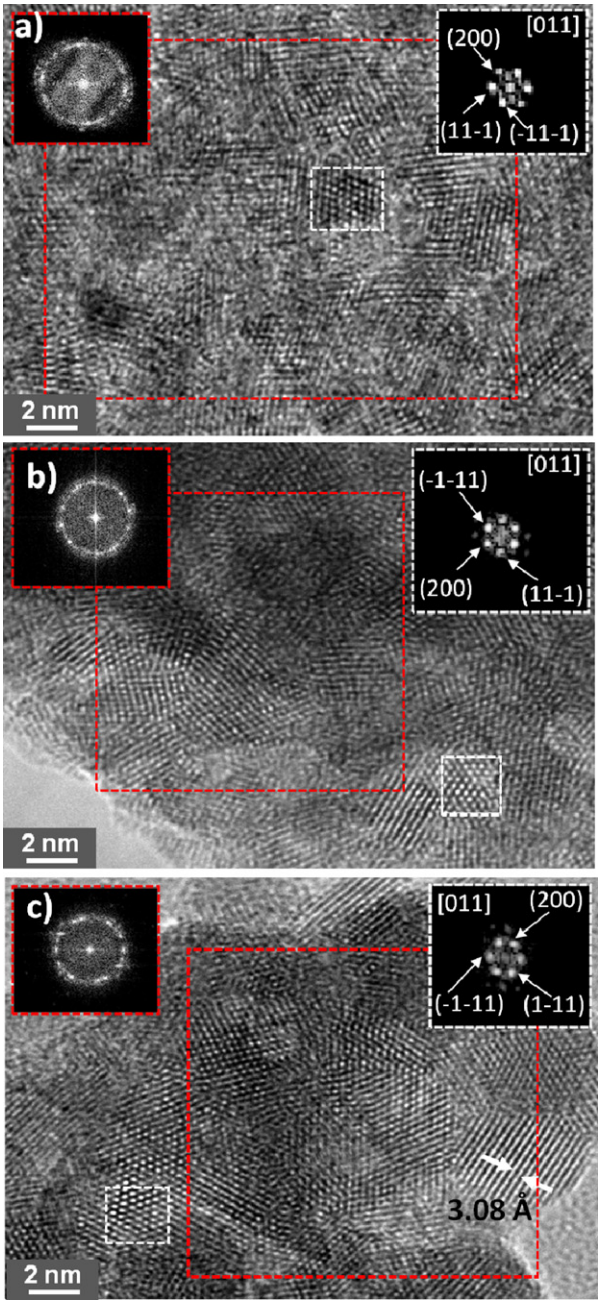

Fig. 6. Representative high resolution transmission electron micrographs recorded for (a) 170 °C, (b) 400 °C and (c) 550 °C erbium–zirconium oxide samples. *Insets*: white dashed squares correspond to DDPs roughly of single nanocrystals; red dashed squares correspond to DDPs taken over larger areas. (For interpretation of the references to color in this figure legend, the reader is referred to the web version of the article.)

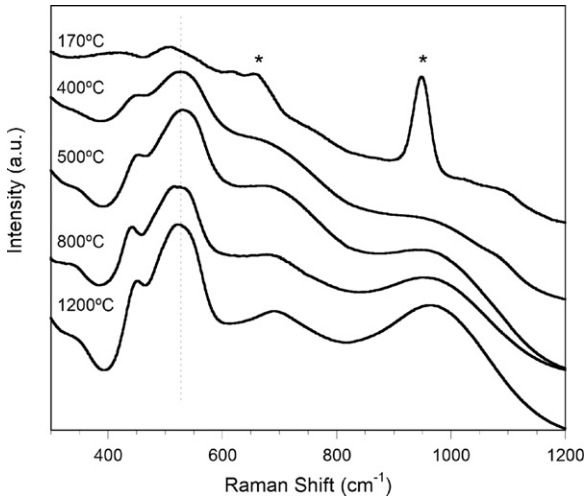

Fig. 7. Raman spectra of the erbium–zirconium oxide samples after annealing at 170 °C, 400 °C, 550 °C, 800 °C and 1200 °C. (*) Signals marked with an asterisk correspond to vibrations of organic matter.

results obtained in DTA/TG, XRD, SEM and N_2 adsorption experiments.

The analysis of the internal structure of these nanoparticles, by means of fast Fourier transform (FFT) techniques, reveals that they are all crystalline. Thus, digital diffraction patterns (DDPs) corresponding to the small squared areas marked on each figure, and which are included as insets, do show, even for the material after solvothermal process at 170 °C, well defined spots which can be assigned to the [0 1 1] orientation of cubic, fluorite-type crystals. For a better comparison between the different samples, the size of this small area analysis has been kept roughly constant and close to the value of crystallite size in the material with smaller crystals.

It is important also worth commenting that the ring-like aspect of DDPs taken over larger regions of the agglomerates (large squares marked in Fig. 6) do confirm this crystalline nature of the particles and also indicate that the oxide nanoparticles are randomly oriented to each other. The rings observed on these large area DDPs can be mostly assigned to the {1 1 1}, {2 0 0} and {2 2 0} interplanar distances of a fluorite structure.

The nanocrystalline nature of the agglomerates is the reason why XRD patterns show very broad peaks. Although it is difficult to precise the dimensions of these nanoparticles, due to their overlap in the HRTEM images, measurements on a large number of crystallites imaged along the edges provided an estimation for the particle diameter of 2–3 nm for the sample treated at 170 °C, 3–4 nm at 400 °C and, finally, 5–6 nm at 550 °C. These values are in fairly good agreement with those obtained by Scherrer equation from XRD results. Note also how the increase of crystallite size is evident in the DDPs, which acquire a more spotty-like appearance at the highest temperature.

Most important, we have to highlight at this point that the 1/2 {1 1 1} reflections characteristic of the pyrochlore superstructure cannot be identified in the DDPs. In the samples annealed at 400 °C and 550 °C, given that the crystals are above the critical size for a reliable structural discrimination, these results evidence that solvothermal synthesis leads to agglomerates of fluorite-type erbia–zirconia nanocrystals. Furthermore, the lattice fringes with interplanar distance of 3.08 Å agree with the (1 1 1) plane of the cubic $Er_{0.5}Zr_{0.5}O_{1.75}$ phase. However, as already mentioned, the absence of the extra-spot in the raw sample does not allow discarding the pyrochlore structure due to the small crystal size.

Finally, a Raman spectroscopy study was conducted in order to get insights on the crystalline structure of the raw sample and to confirm that only one phase was present in the microspheres. This technique is essentially sensitive to oxygen-cation vibrations and is an excellent tool to determine the local disorder. Thus, Raman spectroscopic investigation on the erbium–zirconium oxides could provide unequivocal information to distinguish between a defect fluorite and pyrochlore material. The Raman spectra in the reports are generally presented showing the spectral region between 200 and 1000 cm^{-1}, where Raman active lattice phonons are expected. Fig. 7 shows the Raman spectra of the sample after thermal treatment at different temperatures, including those at 800 °C and 1200 °C, where the fluorite structure is well defined.

Extraction of structural information from Raman spectroscopy is potentially hampered by the presence of erbium ions [28], which may give rise to intense f–f luminescence superimposed on underlying Raman bands. In such cases, true structural information is not contained in the Raman part of the spectrum. To confirm or exclude this possibility, spectra were recorded using different excitation energies, and it was adopted the laser pumping at 785 nm as the best excitation source because active ions do not absorb at this wavelength.

In the literature, cubic pyrochlores [29,30], $A_2B_2O(1)_6O(2)$, belong to the space group ($Fd{-}3m$, O_h^7), no. 227, with $Z=8$. The site symmetry is D_{3d} for A and B ions, C_{2v} for the O(1) ions, and T_d for the O(2) ions and six Raman active modes are predicted. On the contrary, cubic fluorites [31], AO_2, belong to the space group ($Fm{-}3m$, O_h^5), no. 225, where $Z=4$. The site symmetry is O_h for the A ion and T_d for the O ion, and a single Raman peak (normal mode F_{2g} at 465 cm^{-1}) is expected for the ideal fluorite structure (ZrO_2).

In our samples, the band centred around 520 cm^{-1} can be assigned to the Raman active mode F_{2g} of O–Zr–O vibrations of a fluorite type structure, in good agreement with the HRTEM results. However, the spectra are broad, thereby indicating that the crystalline domains are small. The profile of the Raman spectra is quite similar for all temperatures, even if the intensity of the bands is different. Taking into account that HRTEM analysis allowed us to unequivocally identify the presence of fluorite at 400 °C and 550 °C, this fact reveals a similar local disorder in the structure in the sample annealed at 170 °C. The different intensities of the spectrum could be associated to the different degree of crystallization and the size of the crystalline domains.

Taking into account all these results and those previously reported [24,32,33], it can be said that a porous and nanometric fluorite-type oxide was prepared by a free-template non-aqueous process. Stabilization of the metal alkoxide sol is achieved by modifying the precursors with chelating organic ligands that also act as directing-structure agents. Ligands such as β-diketonates are hydrophobic, and helps in the stabilization of the inorganic colloids in organic solvents [34], thus they can stabilize dispersions in essentially the same way as surfactants [35]. This chelation increases the reactivity of the alkoxides in hydrolysis-polycondensation, resulting in facile formation of self-assembled micelar aggregates, that can explain the morphology and textural properties of the materials. Thus, porosity can be achieved through the retention of ligands inside the volume of micelles and thus requires inmobilization of ligands. In this mechanism, the metal oxide nanoparticles are formed in organic solvents and crystallization occurs on subsequent hydro/solvo-thermal treatment. The structural characterization by HRTEM, together with other techniques (Raman, XRD, etc.), has been the key to determine the crystalline structure of these nanooxides.

3. Conclusions

This research was addressed to prepare erbium–zirconium oxide in order to shed a light on systems exhibiting defect fluorite and/or pyrochlore structures. The mixed oxide was successfully obtained using a solvothermal method under mild conditions (170 °C). The material resulted to be constituted of well-defined nanosized crystals (~2 nm in diameter) packed into larger agglomerates with spherical morphology. This particular morphology was reached thanks to the addition of organic ligands that control the nucleation-growth mechanism. Another interesting feature of these materials is their textural properties, reaching high values of specific surface area up to ~280 $m^2\,g^{-1}$. This texture can be accounted for the small size of the nanocrystals and the void spaces between them inside the microspheres. The HRTEM microscopy was demonstrated to be an important tool to prove the formation of the fluorite-type phase and not the pyrochlore one. Raman spectroscopy was used to support the results obtained from HRTEM analysis, but specially to provide evidences of the fluorite crystallization in the sample treated at 170 °C, for which characterization by electron microscopy technique was limited due to the small size of the nanocrystals. The powerful combination of these complementary characterization techniques, HRTEM and Raman, has clearly evidenced the presence, after calcination at the three essayed temperatures, of nanocrystals with fluorite structure. No evidence of crystallites with pyrochlore structure has been obtained. Likewise, domains in which these two phases could simultaneously coexist can be also ruled out.

The combination of interesting morphology, textural properties, and the defect structure of the mixed oxide opens new perspectives in the development, by solvothermal route, of materials for applications in catalysis. In this sense, catalytic tests are now in progress.

4. Experimental

The material was synthesized by a solvothermal methodology using zirconium n-propoxide ($Zr(OPr^n)_4$ (Aldrich, 70%) and erbium acetate ($Er(OAc)_3$, Strem, 99.9%) as precursors and absolute ethanol (Scharlau, 99.9%) as solvent. Acetylacetone (Hacac, Alfa Aesar, 99%) was added as chelating ligand that also helped to dissolve the erbium precursor. The adequate amount of erbium reagent to prepare 1 g of $Er_2Zr_2O_7$ was dissolved in a Hacac–EtOH solution (50 mL). The Er/acac ratio was 1:4. Once the erbium precursor was dissolved, Zr-n-propoxide was added and the solution was stirred for 20 min. The final mixture was transferred into a stainless steel autoclave with Teflon cups of 125 mL capacity (Parr acid digestion bombs) and subsequently heated at 170 °C for 4 days. The resulting suspension was centrifuged, thoroughly washed with ethanol and finally with acetone to remove inorganic and organic residues. The as-synthesized powder, with pink color, was milled in an agate mortar and sieved through a 50 μm mesh screen before any further treatment and characterization (firing cycle, XRD, SEM, TEM, etc.). The sample was then annealed at different temperatures (400, 550, 800 and 1200 °C) during 2 h with a heating rate of 5 °C min^{-1}.

Thermal measurements (DTA/TG) were conducted on a TGA/SDTA 850 Mettler Toledo instrument, from 25 to 1200 °C with a heating rate of 5 °C min^{-1}. The experiments were carried out in a 150 mL Pt crucible under air atmosphere. Phase analysis of the samples was performed by powder XRD with a Siemens D5000 diffractometer with Cu Kα radiation. Data were collected by step-scanning from $2\theta = 20$ to 70° with a step size of 0.05° and 10 s of counting time at each step, and accumulating over two XRD cycles. The goniometer was controlled by the "Siemens DIFFRACT Plus" software. The instrument was calibrated with an external Si standard. Scanning electron micrographs were taken on a field emission scanning electron microscope (SEM) Jeol, JSM-7001F model, equipped with a spectrometer of energy dispersion of X-ray (EDX) from Oxford instruments, using the following operational parameters: acceleration voltage = 20 kV, measuring time = 100 s, working distance = 25 mm, and counting rate = 1.2 kcps. The samples for microstructural and microanalysis determinations were recovered with a graphite film. N_2 adsorption–desorption isotherms were collected on a Micromeritics ASAP2020 gas adsorption analyzer at 77 K, after degassing at 150 °C overnight on a vacuum line. The surface area was calculated by the BET method. Raman spectra were recorded with a spectral window of 1800–100 cm^{-1} on a Jasco NRS-3100 laser Raman spectrophotometer ($\lambda_{exc} = 785$ nm). The characterization by HRTEM was carried out in a Jem-2100 LaB_6 (Jeol) microscope, at an accelerating voltage of 200 kV, coupled with an Inca Energy TEM 200 (Oxford) energy dispersive X-ray spectroscopy (XEDS). The powdered samples were embedded in an epoxi resin (Spurrs resin from Pelco®, Ted Pella, Inc.) and polymerized at 60 °C for 12 h. The embedded samples were sectioned by a Leica ultra cut UCT microtome, equipped with a diamond knife. The microtome sections were between 90 and 150 nm thick, judged by the light reflection of each cut when floating in fluid. Thin films were collected over Ni grids coated with a carbon film before TEM observation. Structural analysis of the recorded images was performed by using the Digital Micrograph 3.4.3 suite from Gatan [36]. The digital diffraction patterns (DDPs) reported here correspond to the log scaled power spectrum of the corresponding fast Fourier transforms. The XEDS spectra were recorded with a 2 nm probe size. The spectra were further processed with the help of INCA software, version, 4.05, from Oxford Instruments.

Acknowledgments

This research was supported by the Spanish Government (MAT2008-03479-NAN, MAT2008-00889-NAN and MAT2011-27008) and Bancaixa Foundation-Universitat Jaume I (P1

1B2007-47 and P1 1B2010-36) projects. F.G., V.D.L., M.L.H. and B.J.-L. are especially thankful to Universitat Jaume I, Generalitat Valenciana and Ministerio de Ciencia e Innovación for their respective fellowships and research contracts (predocUJI, "Grisolia" and FPU PhD grants, and "Ramón y Cajal" program). HRTEM images were recorded at the Electron Microscopy facilities of the SCIC from Jaume I University.

Appendix A. Supplementary data

Supplementary data associated with this article can be found, in the online version, at doi:10.1016/j.jallcom.2011.11.099.

References

[1] T. Takahashi, N.Q. Minh, Science and Technology of Ceramic Fuel Cells, Elsevier, New York, 1995.
[2] (a) B.C.H. Steele, Nature 400 (1999) 619;
(b) M. Daturi, C. Binet, J.-C. Lavalley, A. Galtayries, R. Sporken, Phys. Chem. Chem. Phys. 1 (1999) 5717.
[3] E.C. Subbarao, H.S. Maiti, Adv. Ceram. 24 (1988) 731.
[4] D. Yuan, F.A. Kroger, J. Electrochem. Soc. 116 (1996) 594.
[5] M.S. Isaacs, in: A.H. Heuer, L.W. Hobbs (Eds.), Science and Technology of Zirconia, Advances in Ceramics, vol. 3, American Ceramic Society, Columbus, 1981, p. 406.
[6] M. Maczka, E.T.G. Lutz, H.J. Verbeek, K. Oskam, A. Meijerink, J. Hanuza, M. Stuivinga, J. Phys. Chem. Solids 60 (1999) 1909.
[7] M.C. Caracoche, P.C. Rivas, A.P. Pasquevich, A.R.L. Garcia, J. Mater. Res. 8 (1993) 605.
[8] D.J. Kim, H.J. Jung, J. Am. Ceram. Soc. 76 (1993) 2106.
[9] G. Morell, R.S. Katiyar, D. Torres, S.E. Paje, J. Llopis, J. Appl. Phys. 81 (1997) 2830.
[10] F.A. Mumpton, R. Roy, J. Am. Ceram. Soc. 43 (1960) 234.
[11] M.A. Subramanian, G. Aravamudan, G.V. Subba Rao, Prog. Solid State Chem. 15 (1983) 55.
[12] D.J.M. Bevan, E. Summerville, in: K.A.J. Gscheneidner, L. Eyring (Eds.), Handbook of the Physics and Chemistry of Rare Earths, vol. 3, Elsevier Science Publishers, Amsterdam, 1979, p. 496.
[13] J.B. Thomson, A.R. Armstrong, P.G. Bruce, J. Am. Chem. Soc. 118 (1996) 11129.
[14] E.M. Levin, C.R. Robbins, H.F. McCurdie, Phase Diagrams for Ceramists, American Ceramic Society, Columbus, 1964, p. 1999.
[15] D.J.M. Bevan, E. Summerville, in: K.A.J. Gscheneidner, L. Eyring (Eds.), Handbook of the Physics and Chemistry of Rare Earths, vol. 3, Elsevier Science Publishers, Amsterdam, 1979, p. 401.
[16] K.E. Sickafus, L. Minervini, R.W. Gromes, J.A. Valdez, M. Ishimaru, F. Li, K.J. McClellan, T. Hartman, Science 289 (2000) 748.
[17] Y. Zhang, G. Xu, Z. Yan, Y. Yang, C. Liao, C. Yan, J. Mater. Chem. 12 (2002) 970.
[18] (a) M.P. Yeste, J.C. Hernández, S. Bernal, G. Blanco, J.J. Calvino, J.A. Pérez-Omil, J.M. Pintado, Catal. Today 141 (2009) 409;
(b) M. López-Haro, J.A. Pérez-Omil, J.C. Hernández-Garrido, S. Trasobares, A.B. Hungría, J.M. Cíes, P.A. Midgley, P. Bayle-Guillemaud, A. Martínez-Arias, S. Bernal, J.J. Delgado, J.J. Calvino, ChemCatChem 3 (6) (2011) 1015.
[19] M. Martos, B. Julian-Lopez, E. Cordoncillo, P. Escribano, J. Am. Ceram. Soc. 92 (2009) 2987.
[20] R. Jenkins, R. Snyder, Introduction to X-ray Powder Diffractometry, Wiley, New York, 1996, p. 90.
[21] K.S.W. Sing, D.H. Everett, R.A.W. Haul, L. Moscou, R.A. Pierotti, J. Rouquerol, T. Siemieniewska, Pure Appl. Chem. 57 (1985) 603.
[22] M.K. Devaraju, X. Liu, K. Yusuke, S. Yin, T. Sato, Nanotechnology 20 (2009) 405606.
[23] R. Si, Y.-W. Zhang, S.-J. Li, B.-X. Lin, C.-H. Yan, J. Phys. Chem. B 108 (2004) 12481.
[24] B. Julian-Lopez, M. Martos, N. Ulldemolins, J.A. Odriozola, E. Cordoncillo, P. Escribano, Chem. Eur. J. 15 (2009) 12426.
[25] R. Zhang, Q. Xu, W. Pan, C. Lei Wan, L. Hao Qi, H. Zhuo Miao, Key Eng. Mater. 336–338 (2007) 420.
[26] A. Zhang, M. Lü, Z. Yang, G. Zhou, Y. Zhou, Solid State Sci. 10 (2008) 74.
[27] B.P. Mandal, P.S.R. Krishna, A.K. Tyagi, J. Solid State Chem. 183 (2010) 41.
[28] P. Fornasiero, A. Speghini, R. Di Monte, M. Bettinelli, J. Kaspar, A. Bigotto, V. Sergo, M. Graziani, Chem. Mater. 16 (2004) 1938.
[29] M. Glerup, O.F. Nielsen, F.W. Poulsen, J. Solid State Chem. 160 (2001) 25.
[30] R.A. McCauley, J. Appl. Phys. 51 (1980) 290.
[31] T. Montini, N. Hickey, P. Fornasiero, M. Graziani, M.A. Bañares, I. Alessandri, L.E. Depero, Chem. Mater. 17 (2005) 1157.
[32] G. Garnweitner, M. Niederberger, J. Mater. Chem. 18 (2008) 1171.
[33] M. Niederberger, G. Garnweitner, Chem. Eur. J. 12 (2006) 7282.
[34] V.A. Kessler, G.A. Seisenbaeva, M. Unell, S. Hakansson, Angew. Chem. Int. Ed. 47 (2008) 8506.
[35] V.A. Kessler, G.I. Spijksma, G.A. Seisenbaeva, S. Hakansson, D.H.A. Blank, H.J.M. Bouwmeester, J. Sol–Gel Sci. Technol. 40 (2006) 163.
[36] S. Bernal, F.J. Botana, J.J. Calvino, C. Lopez-Cartes, J.A. Perez-Omil, J.M. Rodriguez-Izquierdo, Ultramicroscopy 72 (3–4) (1998) 135.